Multiply twinned structures in unsupported ultrafine silver particles observed by electron diffraction

B. D. Hall, M. Flüeli, R. Monot, and J.-P. Borel
Institut de Physique Expérimentale, Ecole Polytechnique Fédérale de Lausanne, PHB-Ecublens, CH-1015 Lausanne, Switzerland
(Received 21 May 1990)

The structure of small silver particles has been investigated in detail by use of electron diffraction. Particles are produced by the inert-gas aggregation technique and transferred to a diffraction apparatus by a molecular beam of inert carrier gas. There, their structure can be investigated free of interaction with a substrate or contaminants. The small particles are strongly size dispersed and a technique has been developed to analyze the results. Experimental diffraction measurements are compared with linear combinations of calculated diffraction patterns, from several types of structure, covering a range of diffracting domain sizes. It is possible, in this way, to identify a mixture of structures and estimate the size of the corresponding domains. The analysis clearly shows both multiply twinned (icosahedral and decahedral) and fcc particles, in the size range between 20 and 40 Å in diameter, present in the beam. The relative proportions of these depend on the conditions of particle production.

I. INTRODUCTION

Since the late 1960s, when "multiply twinned" structures were first identified in ultrafine metal particles,[1,2] much research into their occurrence, stability, growth, and structure has been undertaken.

The so-called "multiply twinned particles" (MTP's) are of two basic forms, icosahedral[3] and decahedral,[4] and can be considered an assembly of tetrahedral subunits (20, sharing a common summit, for the icosahedron; and 5, sharing an edge, for the decahedron) with each tetrahedron being related to its neighbors by a twin boundary in the common tetrahedral face. Twinning of regular tetrahedra, however, is inadequate to generate either structure perfectly, and a distortion of the cubic basis is needed: to rhombohedric, for the icoshedron; and orthorhombic, for the decahedron.[5]

Early efforts to describe the relative stability of MTP's and small fcc single crystals showed the icosahedron to be energetically favorable at small sizes. This result was reached independently using elasticity theory[6] and by considering total energy as a sum of pairwise interactions in model particles.[7] More recently, an extension to the analysis using elasticity theory, taking into account detailed surface structure and inhomogeneous strain[8,9] has shown the relative stability of the icosahedron to be contingent on the type of surface faceting. The decahedron, which previously was found to be the least stable structure of the three, can be placed as an energetic intermediary, between the icosahedron and the single crystal, if a strongly faceted surface morphology is considered.

Although first observed in samples prepared by condensation of noble-metal vapor onto a substrate,[1,2] MTP's have now been identified in a variety of materials using different preparation techniques. Of special interest to this work is the method of "inert-gas aggregation" in which a "smoke" of small particles is produced by evaporating a metal or semimetal into an atmosphere of inert gas, where homogeneous nucleation occurs. A large number of materials has been prepared in small-particle form this way.[10–12]

The omnipresence of a support or matrix in structural studies of small particles, where the surface energy contribution to stability is important, has led to the development of experiments that investigate the structure of fine particles free in a vacuum. In one such study, a polyicosahedral structure in argon clusters was identified by comparing electron-diffraction measurements, on clusters produced in the supersonic expansion of a molecular beam, with numerical simulations of the physical system.[13]

The present research has been inspired by the work of the late G. D. Stein on the structure of free metal particles in a molecular beam.[14,15] We have used his technique, of combining electron diffraction on a molecular beam with the gas-aggregation method of particle production, to investigate the structure of ultrafine (diameter $\approx 20-40$ Å) unsupported silver particles. The occurrence of MTP's in silver is well documented,[11,16,17] however, we report here direct observations of these structures in free silver particles.

The remainder of this paper, after a description of the experimental apparatus, is concerned with the interpretation of our diffraction measurements. In Sec. III our method of analysis is developed; we proceed by assuming that the experimental diffraction pattern can be described as a superposition of diffraction contributions from domains of structure within the small particles in the beam. Taking the MTP and fcc structures described above, we calculate a series of diffraction patterns for a range of domain sizes. These are then combined, in a fitting procedure, to give the closest agreement with the experimental data. The results of this analysis describe not only the composition of the beam, in terms of the structures present, but also the relative size distributions of the diffracting domains.

The experimental diffraction patterns, fitted diffraction patterns, and size distribution results are then presented in Sec. IV, and discussed in Sec. V.

II. EXPERIMENTAL

The experimental apparatus is shown in Figs. 1 and 2, with Fig. 2 showing more detail of the particle-beam source. A beam of small particles and carrier gas emerges from the source (on the right in Fig. 1) and crosses, at right angles, a 40-kV beam of electrons, giving rise to a Debye-Scherrer–type diffraction pattern. A pair of Helmholtz coils produces a uniform magnetic field in the region of the beam crossing; varying this field causes the rings of the diffraction pattern to sweep across the entrance aperture to the electron-detection system, allowing the electron intensity along a diameter of the pattern to be recorded.

The electron-detection system[18,19] consists of an electrostatic energy filter, to remove electrons not within 2 V of the incident energy; a silicon surface-barrier detector, charge-sensitive preamplifier and counting chain from EG&G ORTEC, and a Hewlett-Packard 310 microcomputer, interfaced to the counting chain. Single electron events are detected and counted by this system, the measurements being made in a direct-counting mode (i.e., a fixed counting time at each diffraction angle).

Downstream from the beam crossing, a shutter mechanism allows us to obtain a sample of particles from the beam by exposing an amorphous carbon-coated electron-microscope grid to the beam flux. The exposure time of the grid to the beam is kept short, ensuring a low particle density on the substrate; a typical center-to-center distance is on the order of 30–40 nm ($\approx 10^{14}$ cluster m^{-2}), and there is no evidence that coalescence occurs. During

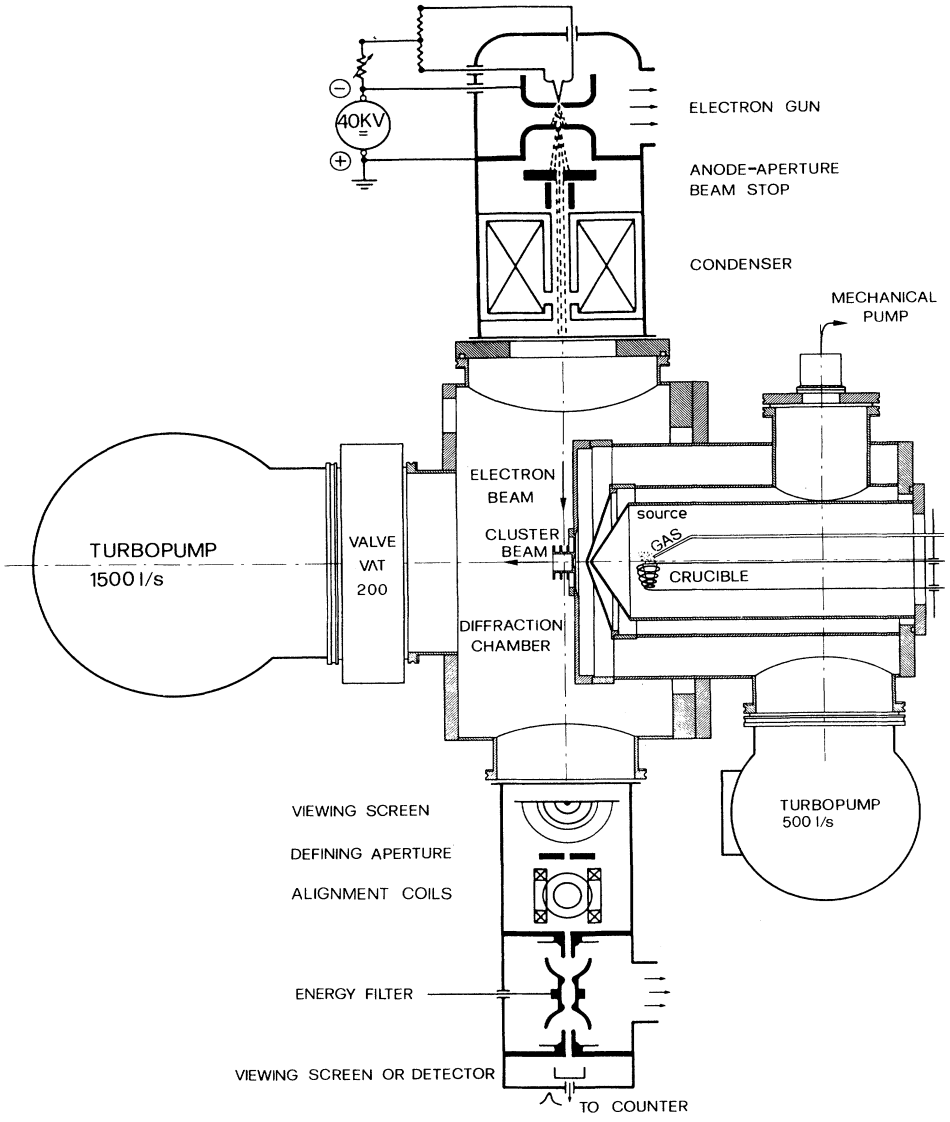

FIG. 1. The electron-diffraction apparatus, with the small-particle source shown on the left. The source and diffraction chambers are labeled, and the intermediate differential pumping chambers (where P_1 and P_2 are measured) can be seen enclosing the source.

TABLE I. Gas pressures in the source (P_{source}), intermediate (P_1 and P_2), and diffraction (P_{diff}) chambers (see Figs. 1 and 2) as a function of the mass flow rate of He (Ref. 20).

Mass flow He [cm^3 (STP)/min]	P_{source} (mbar)	P_1 (mbar)	P_2 (mbar)	P_{diff} (mbar)
750	1.0	0.4	0.9×10^{-5}	3×10^{-6}
1200	1.5	0.7	1.5×10^{-4}	4×10^{-6}
1500	3.0	1.0	3.5×10^{-4}	7×10^{-6}
1700	5.0	2.0	6.0×10^{-4}	1×10^{-5}
2000	10.0	8.0	1.0×10^{-3}	2×10^{-5}

an experiment a number of samples are taken which are later removed from the diffraction chamber and transferred to a microscope (Philips EM 430 ST) for observation. The negatives of the photographic images thus obtained are digitized (Perkin-Elmer PDS 2020 G) and analyzed numerically to obtain the distribution of particle sizes. Special software for this purpose has been developed, with care taken to avoid systematic thresholding errors due to the low particle-to-background contrast in the images. Particle samples, taken at the start and finish of a diffraction measurement, were also used to verify that beam conditions remained stable during a measurement.

Data characterizing our experimental apparatus are given in Table I, which shows the evolution of the pressures in the different chambers of the diffractograph (Fig. 1) as the carrier-gas-flow rate is varied,[20] and Table II (Sec. IV), which summarizes the conditions under which the experiments in this article were made.

The source

The source is based on an earlier one of Stein's[14] and has been designed with his collaboration. Small particles are formed by inert-gas aggregation in the inner "source" chamber. This mixture of carrier gas and small particles is extracted, through a series of orifices separating differentially pumped chambers, into the diffraction chamber, which it enters as a supersonic flow of inert gas containing small particles. Differential pumping, between the source chamber and the diffraction chamber, removes a substantial proportion of the carrier gas from the beam, improving the sensitivity to the diffracted intensity from the small particles.

Nucleation and growth occur in the inner chamber (see Fig. 2), where an inert gas, initially at room temperature, mixes with hot metallic vapor. As it cools, the vapor forms a region of high supersaturation above the crucible, favoring nucleation there. Strong convection in this chamber prevents a detailed analysis of the nucleation conditions;[21] however, trends in particle size can be predicted. The average particle size can be expected to vary in the same way as the product P_0T_0, where P_0 is the inert-gas pressure and T_0 is the evaporation temperature. An increase in P_0T_0 will produce larger particles; a decrease, smaller particles.[14] The parameters P_0 and T_0 are

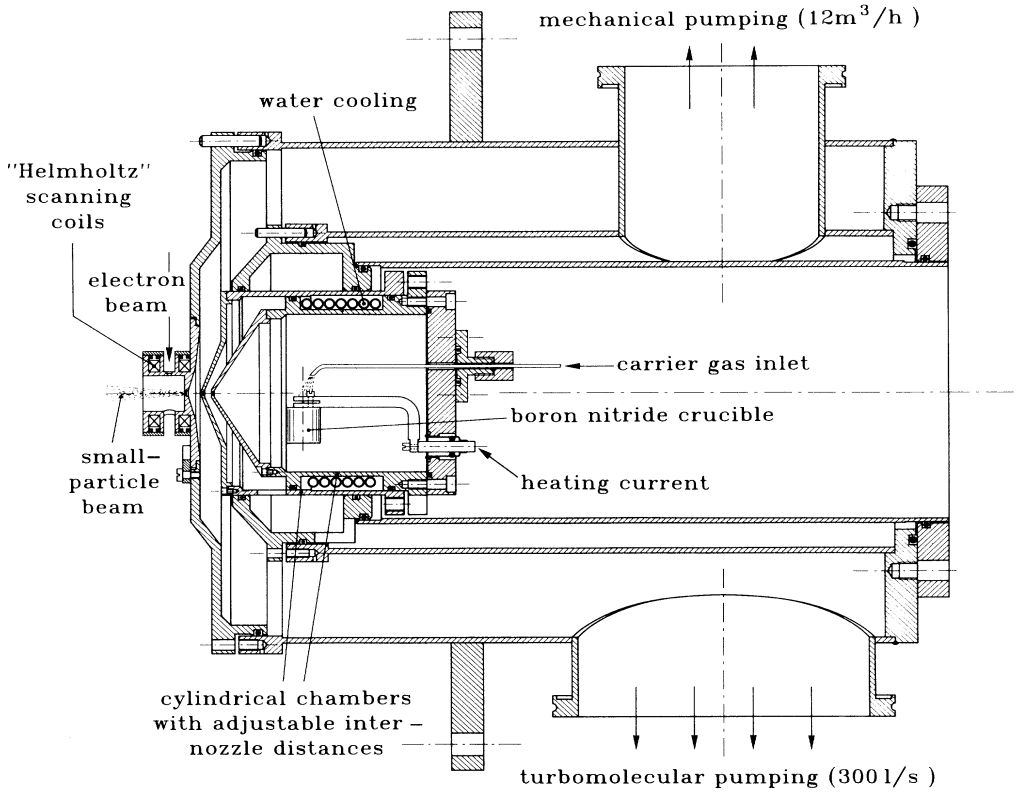

FIG. 2. Detail of the source chamber and differential pumping stages leading to the diffraction chamber.

adjusted interactively during an experiment, giving some control over the particle size distribution.

The sensitivity of evaporation rate to temperature has led us to install a closed-loop control system to stabilize the temperature against drift.[22,23] A thermocouple, embedded in the crucible, is used to estimate the evaporation temperature, and, by regulating the crucible power supply, thermocouple temperature fluctuations have been reduced to $\pm 0.5\,^{\circ}\mathrm{C}$. This effectively suppresses variations in particle-beam intensity, due to a changing evaporation rate, during the time required to measure the diffraction pattern.

Two other source parameters are used to influence the nucleation conditions and hence the size of the particles. The choice of carrier gas can change the position of the nucleation region with respect to the evaporation source; a heavier gas will tend to limit diffusion of the metallic vapor and provide more efficient cooling, so nucleation will occur in a region of relatively higher vapor density, producing larger particles.[24] In all of the results to be presented in this paper, helium has been used as the carrier gas; argon and nitrogen have also been tried. however, in accord with the simple model of Wada,[24] these gases were found to favor the growth of larger particles, which were of little interest to this study.

A second factor affecting particle growth is the gas-flow rate in the source chamber; changing the diameter of the source chamber exit nozzle will cause the average flow rate in the chamber to vary, affecting the time a particle is likely to spend in the nucleation region. Hence an increase in the flow rate (larger nozzle diameter) will reduce the size of particles produced.[25]

The dimensions of the nozzles have been optimized and remain the same (with one exception: the source nozzle diameter; see Table II) for the data presented below. All nozzles are made from graphite, which has been found to reduce the rate of accumulation of silver deposits (clogging).[21] The first nozzle, at the source chamber exit, is cylindrical, with a diameter of 4 mm and a length of 8 mm. This geometry improves the collimation of the beam, reducing clogging in the following nozzle. The second nozzle is conical, opening with an angle of 20° and a minimum throat diameter of 1.5 mm. This geometry is also effective in reducing clogging. The final nozzle, through which the particle beam enters the diffraction chamber, is a simple diaphragm 1.5 mm in diameter.

The size-distribution data obtained by electron microscopy allows an estimate of the particle flux to be made, typically $\approx 10^{11}$ clusters s^{-1}. Furthermore, using an estimate of the particle velocity and the measured beam dimensions, it is also possible to calculate an equivalent particle number surface density by projecting the cluster density in the beam onto a plane normal to the incident electrons. This shows how sensitive electron diffraction is when applied to a beam of particles: a typical value $\approx 10^{12}$ clusters m^{-2} is 4 orders of magnitude less than supported sample densities commonly employed.[19]

III. ELECTRON DIFFRACTION AND NUMERICAL ANALYSIS

The distribution of intensity in the Debye-Scherrer rings, provided kinematic diffraction conditions hold and only one type of atom is present, can be expressed with the Debye equation,[26]

$$I(S)=f^2(S)\sum_{i,j}\frac{\sin(2\pi S r_{ij})}{2\pi S r_{ij}}\ , \tag{1}$$

or, alternatively,

$$I(S)=Nf^2(S)\left[1+\int_0^{\infty}4\pi r^2\rho(r)\frac{\sin(2\pi Sr)}{2\pi Sr}dr\right]\ , \tag{2}$$

where $S=2\sin\theta_B/\lambda$, λ is the electron wavelength; θ_B is the Bragg angle; r_{ij} is the distance between atoms i and j; $f(S)$ is the atomic scattering factor; and $\rho(r)$ is defined so that $4\pi r^2\rho(r)dr$ is the average number of atoms in the volume element $4\pi r^2 dr$ around an atom in the cluster [i.e., $\int_0^{\infty}4\pi r^2\rho(r)dr=N-1$, with N the number of atoms in the cluster].

Equation (2) is a three-dimensional Fourier transform of $\rho(\mathbf{r})$ that reduces to an integration over a single scalar variable, r, because of the spherical symmetry that is introduced by random orientation of particles in the beam.

We proceed with two rather different approaches to investigate ordering in the interatomic distances; both will be combined in the final analysis of our results. The first attempts to calculate $\rho(r)$ by direct inversion of the measured intensity, $I(S)$; the other uses the Debye equation (1) to calculate the diffraction patterns of several possible structures, which can then be compared with the experimental results.

A. Fourier inversion of experimental data

It is convenient, when analyzing the structural information contained in diffraction measurements, to transform data back into real space. Fourier inversion of the experimental values of $I(S)$ provides an estimate, $\hat{\rho}(r)$, of the function $\rho(r)$. However, to be reliable this inversion procedure must be handled carefully, and a wide angular range of diffraction measurements is essential.[27] In this subsection we discuss the effect, on $\hat{\rho}(r)$, of restricting the range of diffraction angles over which $I(S)$ is measured. In our data the information content of $\hat{\rho}(r)$ is insufficient, in itself, to use to analyze the small particles' structure, although it does provide a valuable estimate of their lattice parameters, which is incorporated in our later analysis.

The intensity $I(S)$ is only measured on a small interval of S: $S\in[S_{\min},S_{\max}]$, so when inverting Eq. (2) the experimental constraints can be expressed as finite integration limits. The inverse Fourier transform of Eq. (2) takes the form

$$\hat{\rho}(r)=\int_{S_{\min}}^{S_{\max}}4\pi S^2\left[\frac{I(S)}{Nf^2(S)}-1\right]\frac{\sin(2\pi Sr)}{2\pi Sr}dS\ . \tag{3}$$

From Fourier theory, the effect of finite integration limits can be considered a restriction to the low- and high-frequency Fourier components of the function $\rho(r)$, and so $\hat{\rho}(r)$ will be band limited. Features in $\rho(r)$ whose characteristic dimensions are either greater than $1/S_{\min}$ or less than $1/S_{\max}$ will be distorted or even completely

eliminated by the absence of high- and low-spatial-frequency components, respectively, in $\hat{\rho}(r)$. The small-S cutoff, $S_{\min}$, limits the slowly varying components of $\rho(r)$, while $S_{\max}$ limits rapid components.

In electron diffraction the incident electrons interact with the electrostatic potential of the diffracting body, the spatial variations in this potential being reflected in the angular distribution of diffracted electron intensity. The slowest spatial variation can be associated with the average electrostatic potential, which changes abruptly at the surface of a small particle. This component gives rise to the intensity at small angles in the diffraction pattern, which is related to the external form of the particles.[26]

Other than the external shape of the small particles, no structural information is contained in the small-angle data; it is, however, indispensible, when calculating $\rho(r)$ for isolated particles, to take into account the diffracted intensity at small angles. The finite extent of $\rho(r)$ expresses the presence of a surface, which determines the average coordination of atoms in the particle. If the small-angle data are left out, distortions to $\hat{\rho}(r)$ will result and lead to systematic errors in estimates of both coordination numbers and neighbor separations. To see why, consider a diffraction pattern from a hypothetical small particle in which the diffracted intensity is confined to small angles alone. Such a pattern would arise if the particle was of strictly uniform density (i.e., no atoms), so that $4\pi r^2\hat{\rho}(r)$ would be without structure, and tend to zero as r approaches the diameter of the particle. If density variations are then introduced, without changing either the external particle shape or the average density, the diffraction pattern at small angles remains unchanged, while, at larger angles, diffracted intensity will begin to appear, reflecting the particle's internal structure. The form of $4\pi r^2\hat{\rho}(r)$ retains the previous "small-angle" form as a bounding envelope, but now also shows the structure introduced.

In our data, $S_{\min}$ is such that diffracted intensity at small angles has not been measured. In order to correct for this loss of information, we use the measured size distribution, which is available from the supported particle samples extracted from the beam (see Sec. II), to generate, analytically, small-angle diffraction data in the region $S\in[0,S_{\min}]$. We do this by assuming a spherical shape for all particles and obtain, using Eq. (2), the form of $I(S)$ as a function of particle diameter.[26] It is then straightforward to integrate this function over the distribution of sizes for each experiment, thus estimating the form for the small-angle scattering.

Equation (3) can now be written

$$r\hat{\rho}(r)=2\int_0^{S_{\max}} S\left[\frac{I(S)}{Nf^2(S)}-1\right]\sin(2\pi Sr)dS\ , \tag{4}$$

where the analytic form for $I(S)$ is used to remove the nonzero lower integration limit.

The remaining integration limit, $S_{\max}$, causes the sharp features of the original function, $\rho(r)$, to broaden in $\hat{\rho}(r)$, due to the lack of rapidly varying components. The characteristic dimension of broadening is $\sim 1/S_{\max}$. From the convolution theorem of Fourier transforms, we can write

$$r\hat{\rho}(r)=[r\rho(r)]*\mathcal{W}(r)\ , \tag{5}$$

where "$*$" is the convolution product and $\mathcal{W}(r)$ is the Fourier transform of the function that restricts $I(S)$ to $[0,S_{\max}]$. We write

$$\mathcal{W}(r)=\frac{\sin(2\pi S_{\max}r)}{2\pi S_{\max}r}\ . \tag{6}$$

This convolution product not only broadens features from $4\pi r^2\rho(r)$, but will also introduce a compounding background term; every peak in $4\pi r^2\hat{\rho}(r)$ contributes an oscillatory term that is roughly constant in amplitude and extends to the right of the peak, towards increasing r. This background therefore depends on the features in $4\pi r^2\rho(r)$. Suppose, for example, that $\rho(r)$ consists of a single interatomic distance, r_0; $r\rho(r)$ will consist of a δ function at r_0 and $r\hat{\rho}(r)$ will take the form $\mathcal{W}(r-r_0)$. Now, $\mathcal{W}(r-r_0)$ falls off as $|r-r_0|^{-1}$ on either side of the maximum, which means that $4\pi r^2\hat{\rho}(r)$ will tend to an oscillating term of constant amplitude with increasing r. A solution to this undesirable effect is to multiply the $I(S)$ data with a window function whose Fourier transform, $\mathcal{W}(r)$, rolls off more rapidly on either side of the central maximum (see, for example, Ref. 28). However, such window functions have the disadvantage that the steeper roll-off is accompanied by an increase in the central maximum broadening, reducing the resolution of details in $4\pi r^2\hat{\rho}(r)$. No window function has been used in the treatment of the results presented here.

The restricted range of S values ($S\in[0.3,0.9]$ Å^{-1}) for which it has been possible to obtain the experimental diffraction data presented in this paper excludes the use of direct inversion as a single reliable means of interpretation of our data. Only the position of the nearest neighbors can be determined with accuracy. This is because the first peak in $4\pi r^2\hat{\rho}(r)$ is well separated from the second (1.2 Å in the fcc structure of silver), which corresponds to the second coordination shell, and because the first peak is not affected by the type of background interference described above, there being no other peaks at lower values of r. Knowledge of the average nearest-neighbor distance in the clusters is nevertheless essential in providing an estimate of the lattice parameter for each experiment. This information has been incorporated in the construction of model structures, and will be referred to again in Sec. IV.

B. The diffraction pattern from model structures

The limited information obtainable by direct inversion of the diffraction pattern does not preclude the extraction of useful structural data from our results. The relative failure of the direct approach is a consequence of its insensitivity to the physical constraints of the problem: *a priori*, any combination of interatomic distances, be they physically reasonable or not, can be obtained by the Fourier transform. Low resolution only reflects a large number of possible configurations and insufficient information with which to differentiate between them. A

promising approach to this problem is the application of the "maximum-entropy method" to the inversion of the diffraction data.[29] However, here we have adopted a more direct technique.

Our analysis proceeds by considering only distinct types of structure, thereby limiting the combinations of interatomic distances, and determining a set of these structures that most closely resembles our measurements. This is not a new idea; the Debye equation (1) has been used extensively, in the past, to calculate the diffraction patterns corresponding to models of structure (see, for example, Refs. 30 and 31). The allure of these calculated diffraction patterns can then be compared directly with results obtained by experiment. The structures of amorphous metals, for example, have been studied in this way (see Ref. 32 for a review). However, it is implicit in this method that the disordered regions outside domains of coherent structure, and neighboring domains with different orientation will contribute no new features to the diffraction pattern. This hypothesis has been tested in numerical simulations using the Debye equation, and it is upheld when there is no angular correlation between neighboring domains.[33,34]

Twinned domains are, however, strictly related, and in the case of silver they must also be considered. To illustrate the effects of a single twin boundary on the diffraction pattern, we have simulated the diffraction from a small spherical particle, 42 Å in diameter, with fcc structure and a twin plane passing through its center. The diffraction pattern (Fig. 3), normalized by the number of atoms in the cluster, is compared with two other patterns both from monocrystals: one, bounded by a sphere, is the same size as the twinned particle; the other, a hemisphere, is the size of a single fcc domain in the twinned particle. The diffraction from the smaller fcc monocrystal is a better fit to the pattern from the twinned particle, the widths and heights of the (200), (220), and (311) peaks agree well, and only the (111) peak intensity is noticeably smaller. A detailed discussion on the diffraction from small silver particles containing stacking faults has been given by Kimoto.[10] It can be shown that, for the fcc reflections present in our data, only a fraction of the (111), (222), (220), and (311) planes are continuous across a twin plane, leading to diffraction from such a particle that is more closely characterized by the size of its domains than by its entire volume.

For this work, it has been necessary to choose a limited number of structure types, which are likely to present the conditions of local order in our samples. Our choice of structures has been limited to the icosahedra, decahedra, and fcc cubo-octahedra described in the Introduction (the assertion that twinned particles can be fitted by their constituent domains is discussed further in Sec. IV). We have considered a range of sizes (diameters up to ≈ 60 Å) by generating a series of clusters, each with the same geometrical shape, but with an increasing number of atoms. The atomic coordinates were determined according to relaxed models described by Ino,[6] and the corresponding diffraction patterns were calculated using these static atomic positions.

The small size of these model clusters introduces broadening in the features of the diffraction pattern, which is easily seen when diffraction patterns from different-sized particles are compared (see Fig. 4). For MTP's, because of the absence of a periodic basis in real space, it is not possible to think of size broadening in the same terms as for a small single crystal. The broadening of diffraction features is better understood as an absence of high-frequency terms in the Debye equation (1), due to the upper limit on the interatomic distances.

Coupled with broadening, diffraction from very small particles can show new features that are related to their

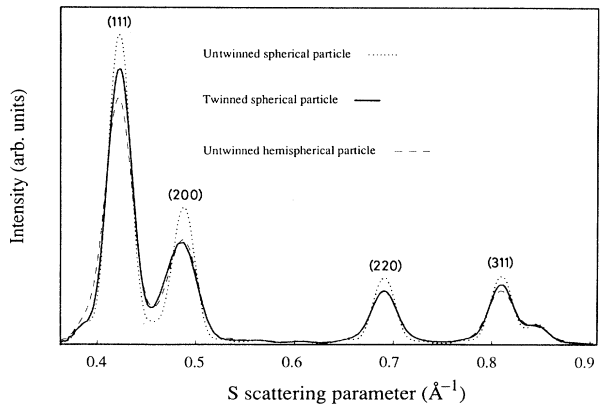

FIG. 3. Stimulated diffraction patterns for a simply twinned spherical particle, 42 Å in diameter, and two untwinned fcc particles: one, the same size and shape as the twinned particle; the other, a hemisphere, equivalent to a single fcc domain in the twinned particle. Each figure has been normalized, for the purpose of comparison, by the number of atoms in the cluster.

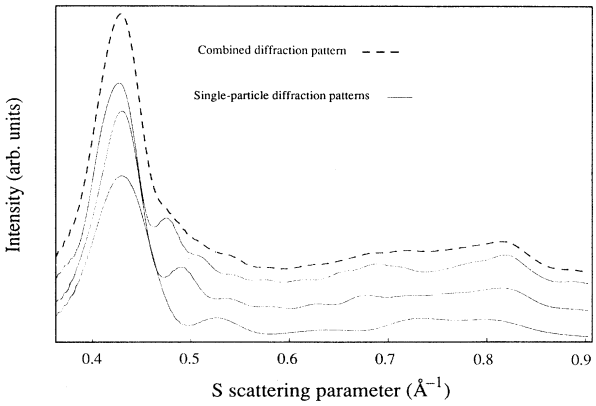

FIG. 4. Three simulated diffraction patterns for icosahedral clusters 17, 26, and 36 Å in diameter. Each curve has been normalized by the number of atoms in the cluster, and the origin shifted vertically (the 17-Å cluster is closest to the x axis, followed by the 26-Å, and then the 36-Å cluster) to enable easy comparison of the diffraction features. The dotted curve is the direct sum of the three normalized patterns, rescaled for comparison.

external form. This is particularly pronounced in the icosahedron (Fig. 4), where a satellite peak is apparent to the right of the first diffraction maximum. This satellite shifts as the size of the icosahedron is varied, moving closer to its large neighbor as the particle diameter is increased from 17 to 26 to 36 Å. Note, also, the varying position of the first strong diffraction peak; this is not related to a change in interatomic distances, which are identical for each of the simulations

Although it is tempting to compare experimental data with individual model patterns in order to identify structures, some caution is required in doing so because of the size-dependent diffraction features. In an earlier publication[35] we mistakenly rejected the presence of icosahedra in our beam, due to poor agreement between simulated and experimental data. We now realize that when diffraction patterns containing domains of different sizes are combined, the individual size effects can contribute to broadening as well as changing a peak's profile. This can be seen in Fig. 4, where the three icosahedral simulations are added together. It is essential, when describing our experimental data, to include not only a variety of possible types of structure, but also to consider how the diffraction patterns from these will combine when a size range of small diffracting domains is present.

Clearly, if an analysis of the experimental data is to be made by comparing measured and calculated diffraction patterns, it will be necessary to consider combinations of the calculated patterns. Such combinations must superpose the calculated diffraction patterns in proportion to the distribution of domain sizes, and, if necessary, include a mixture of structure types. Provided the models of structure used closely approach the reality, an excellent approximation to the experimental diffraction pattern will then be obtained.

C. Fitting models to experimental diffraction patterns

The development of the preceding subsection leads naturally to the possibility of fitting a complex diffraction pattern with a combination of simulated ones from structure models. It seems reasonable to expect that the domain size distribution as well as structural information can be extracted from the diffraction pattern of such small particles, because of the prominence of size related features.

Twelve clusters of each type, the largest being ≈ 60 Å in diameter, have been used to generate the diffraction patterns used in the fit. These figures were then combined in proportions determined by a size-distribution function, one of which was associated with each type of structure. The form of these size-distribution functions was varied during the fitting, changing the relative contributions of each simulated diffraction pattern to the total pattern. A least-squares criterion, based on the difference between the trial function and the experimental diffraction pattern, is used as a figure of merit for fitting. In this way different combinations of structure were investigated and the best approximation retained.

In an initial attempt at minimization, a multidimensional simplex fitting routine[36,37] proved to be unsatisfactory. The simplex, which looks for the steepest descent in its neighborhood, became easily trapped by shallow minima in the response surface. A "simulated annealing" algorithm,[38,37] which is less sensitive to the local structure of the response surface, was able to avoid this problem and consistently converge towards a reproducible solution.

Our implementation of the annealing method uses a random walk in the multidimensional space of the size-distribution parameters. At each step the new configuration will be accepted or rejected according to the difference in the values of the response surface (figure of merit), ΔE, between the old and new configurations. If $\Delta E \leq 0$, meaning that the new position is a better fit than the old, the step is accepted. If $\Delta E > 0$, the step is accepted with probability $P(\Delta E) = \exp(-\Delta E/kT)$, analogous to the Boltzmann factor in statistical mechanics. The parameter kT is chosen large enough, at the beginning of a fit, so that nearly all steps in the random walk are accepted. Then, by reducing the temperature gradually enough it is hoped that the global minimum will "condense" out as a preferred combination of structures.

The annealing technique, by its statistical nature, does not guarantee a solution corresponding exactly to the global minimum. However, it is considerably more robust that steepest-descent techniques, like the simplex. It is possible to test the uniqueness of a solution by fitting the same data using different initial conditions. Random generation of a starting point, which will determine the resulting walk in the configuration space, allows us to test the reliability of our solutions by rerunning the fitting procedure several times. The results have always been stable, showing that there are no other combinations of small-particle diffraction patterns that might equally well fit the experimental data.

IV. RESULTS

A series of five experimental diffraction patterns has been chosen, covering the range of diffraction profiles we have observed in our experiments; these are shown in Figs. 5–9. The corresponding experimental conditions, and statistics associated with the fitting analysis, are presented in Table II. These include the third moment of the respective size distributions; the relative proportions of each structure type, found by fitting; and the third moment of the experimental size distribution. The third moment is used because the intensity diffracted from a domain is proportional to its volume.

Also shown in these figures is the function obtained as the best fit to the diffraction pattern, and the composition of this function in terms of the structure types. The size distribution obtained by electron microscopy (upper histogram) can be compared with the total of the domain size distributions obtained from the fit (open bars in the three lower histograms), which, in turn, can be compared with the size distribution of each structure type (solid bars).

The diffraction patterns have been corrected for background scattering due to the residual and carrier gases in the diffraction chamber. This correction term is found by

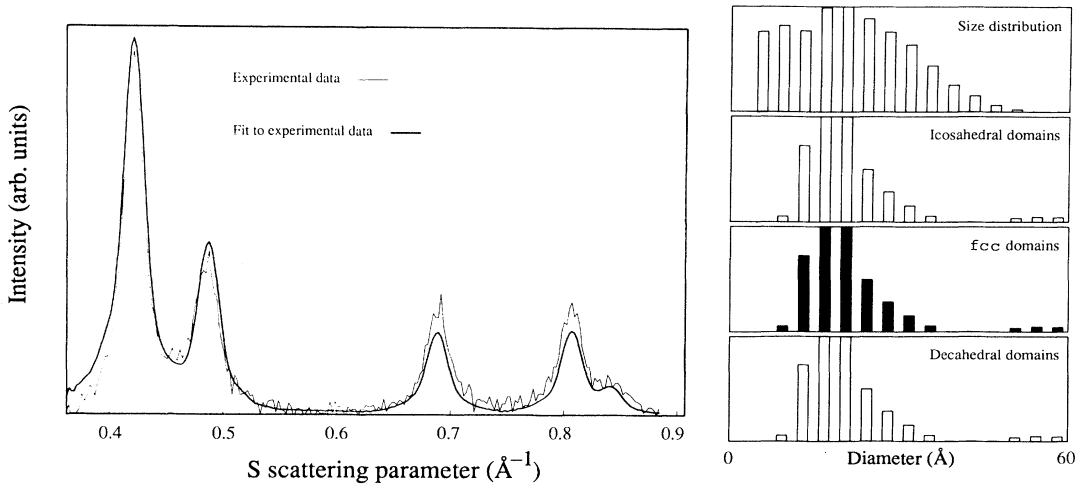

FIG. 5. Figures 5 to 9 show experimentally measured diffraction patterns and best-fit simulations. The histograms show the experimental size distribution (top), the total domain-size distribution (lower histograms with open bars), and the relative contributions of each structure type to the total (solid bars). The corresponding source conditions and statistics of the size distributions are reported in Table II.

measuring the diffracted intensity from a beam of carrier gas that is free of particles and under conditions, of source and diffraction chamber pressures, which are similar to the experiment. The gas-diffraction pattern is a monotonically decreasing function of scattering angle; after measurement it is smoothed and then subtracted from the experimental data.

Before fitting, the experimental data were inverted, as described in Sec. III A, in order to estimate the nearest-neighbor distances in the clusters. With this estimate it was then possible to scale the model structures—the equivalent of a homogeneous contraction or expansion—so that they too had the same average nearest-neighbor separation. The fitting procedure used these appropriately scaled models.

One cautionary remark is appropriate concerning the presence of large icosahedra. As mentioned above (Sec. III B), twinned particles are best fitted by monocrystals the size of an untwinned domain. However, when fitting a twinned particle to a combination of possible structures, an icosahedral contribution helps to compensate for the intensity deficit in the (111) reflection. During testing of the fitting procedure, this artifact was observed in simulated samples of twinned particles. The icosahedral contribution in such cases is small and appears at sizes very much greater than the fcc domains

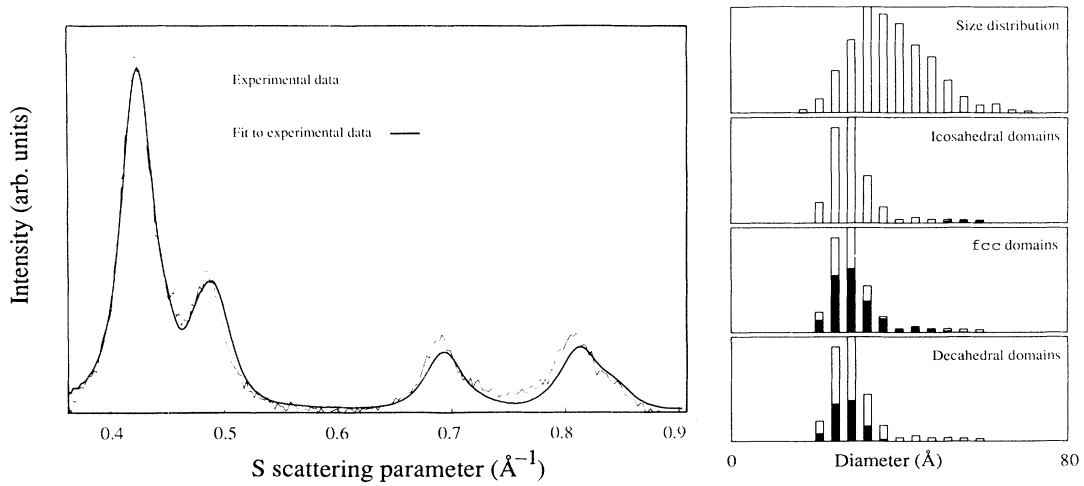

FIG. 6. See Fig. 5 caption.

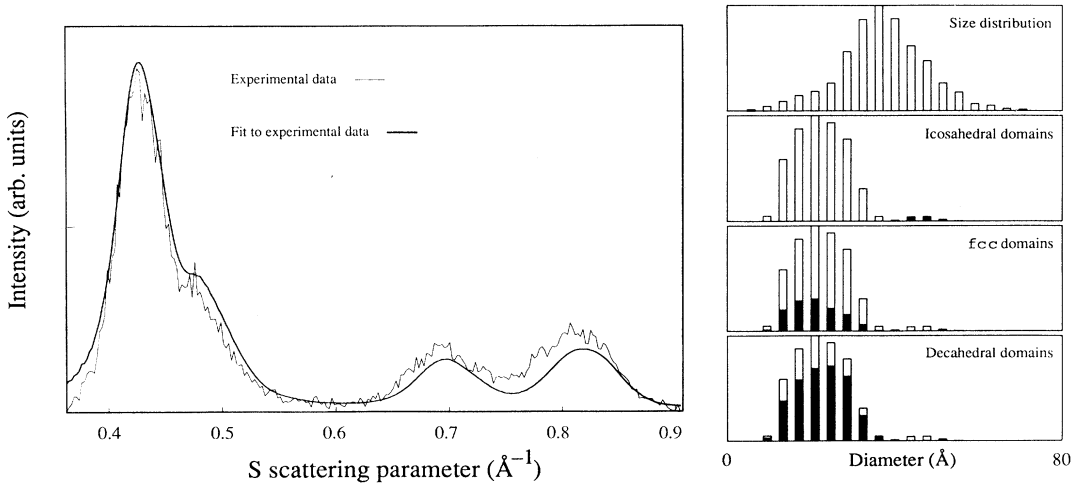

FIG. 7. See Fig. 5 caption.

chosen by the fit. We therefore ascribe the icosahedral components in Figs. 6 and 7 to the presence of fcc twins. Furthermore, the icosahedral domain size distribution is likely to be slightly skewed towards large diameters by this artifact, and this will appear in the third moment of the distributions.

V. DISCUSSION

The order of presentation of the figures has been chosen according to the evolution of the diffraction features on the right-hand side of the diffraction pattern [between the (220) and (311) fcc reflections]. The detailed analysis shows that a gradual change in composition is taking place. Starting from a pure fcc sample, the presence of an increasing number of decahedra tends to broaden the diffraction peaks and to fill the region between them. As this trend continues, and the diffracted intensity at higher angles become continuous, the dominant structure is seen to shift from decahedra to icosahedra.

The quality of the diffraction patterns generated by simulated annealing is encouraging: the form and position of the first diffraction peak is well represented, as is the allure of the diffraction at higher angles. There appears to be a small consistent intensity difference at higher angles, where the fitted function falls below the experimentally observed diffraction intensity.

A refinement to the model diffraction patterns might improve the fit: Instead of the abrupt boundary condition (discrete domain size), which gives rise to rather marked size-dependent features in the diffraction pattern, a probability function of interatomic distances could be used to delimit a diffracting domain,[39] thus further allowing for a

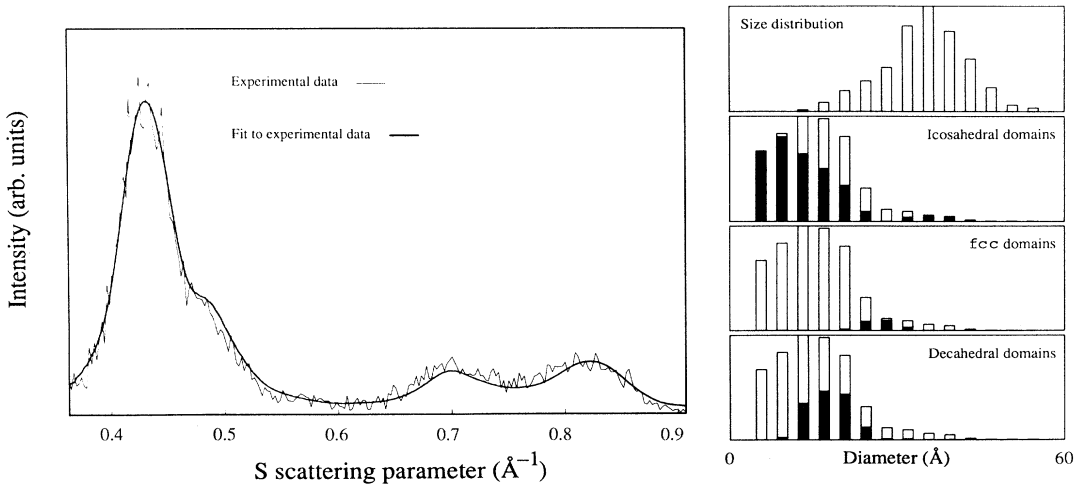

FIG. 8. See Fig. 5 caption.

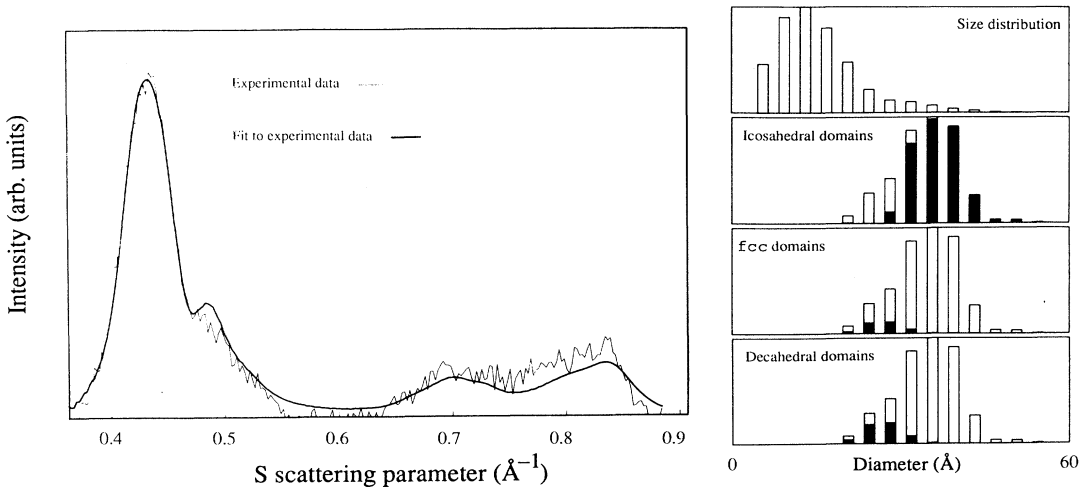

FIG. 9. See Fig. 5 caption.

continuous distribution of cluster or domain sizes.

A possible source of error is the use of kinematical diffraction theory to describe the diffraction from silver particles as large as 50 Å in diameter. If dynamical effects are present, they could give rise to an attenuation in the intensity of diffraction peaks at smaller scattering angles, which is consistent with the tendency observed. They might also affect the average intensity diffracted from clusters as a function of size, leading to an error in the relative proportions of cluster domain sizes found by fitting.

Variations in relative integrated peak intensities, due to dynamical effects, have been investigated by de Boer and Stein.[15] Their study used an appropriately weighted sum of calculated diffraction data, from a series of infinite-crystal slabs oriented over a range of angles with respect to the beam axis, to estimate the diffracted intensity for small randomly oriented particles. By varying the slab thickness, they investigated the relative variation in the intensity of a number of diffraction peaks as a function of particle size. The calculations used the "multislice" method and took absorption into account. Their results show that in the worst case [the (111) peak], over the range of sizes we are considering, the variations in integrated intensity will be no more than about 10%. Thus, the profile of the diffraction patterns will not be seriously distorted.

Systematic changes in the average diffracted intensity, common to the diffraction peaks of interest, may also occur, in which case larger clusters may diffract weakly compared to the predictions of kinematical theory, and thus be underestimated in the analysis of the beam composition. To estimate this effect we refer to the original calculations of Blackman,[40] which can be considered a reliable first estimate of the deviation from kinematical diffraction in small randomly oriented particles.[41] According to Blackman, for 50-Å particles, there will be an average drop of around 15% in the integrated peak intensities. This, therefore, may give rise to a slight bias towards smaller diffracting domains in the results of our fitting analysis, but should not distort the overall trends observable in the domain size distributions and structures.

When looking at the results of the analysis in terms of size distributions, two points should be kept in mind. The fitting procedure is applied directly to the diffraction data, in which the contribution to the diffracted intensity from each domain depends on the domain's volume. It follows that only the larger diffracting domains will contribute sufficient intensity to be detected by fitting. This

TABLE II. Source conditions and size distribution statistics: ϕ_V is the third moment of the size distribution (in Å), and % is the percentage of each structure type. Entries marked with a dagger were made using a 6-mm source-nozzle diameter.

	Source		Fitted distributions							Experiment
			Decahedra		Icosahedra		fcc		Total	Total
Figure	P_0 (mbar)	T_0 (°C)	ϕ_V	(%)	ϕ_V	(%)	ϕ_V	(%)	ϕ_V	ϕ_V
5	2.0	1167	0	0	0	0	37	99	37	32
6†	1.5	1228	26	33	55	2	32	63	35	44
7†	2.7	1137	24	70	45	2	23	27	28	44
8	2.0	1227	19	29	28	65	26	5	25	38
9	3.8	1147	26	12	37	79	26	7	36	50

is clearly the case in Fig. 9, where the experimental distribution peaks at a much smaller size than the fitted distribution. In fact, the third moment of the experimental distribution is even higher than the fitted one (see Table II), showing that the particles far to the right of the maximum in the size distribution determine the form of diffraction pattern observed.

Secondly, when comparing the domain- and particle-size distributions, the domain size must, by definition, be less than or equal to the particle size itself. Hence when the domain distribution closely approaches the size distribution, as in Fig. 5, the domains are probably representative of the single-particle structure. On the other hand, a significant difference between distributions, as in Figs. 7 and 8, points to an important proportion of particles in which the domain size is considerably smaller than the particle.

High-resolution electron microscopy has been performed on some of the supported samples extracted from the beam. Although a systematic comparison has not been undertaken, inspection of the images reveals both icosahedra and decahedra, as well as fcc monocrystals. Many of the particles, however, exhibit complicated forms, indicating that their internal structure is subdivided. The classification of these complicated structures has not been attempted.

The nucleation conditions should be considered quite different for each experimental figure. The pressure and temperature alone (Table II) are largely insufficient to describe the behavior of the source between experiments, which is extremely sensitive to such factors as gas-inlet position and orientation, and crucible position. It has never been possible, in a single experiment, to obtain the entire range of diffraction patterns presented here; however, by varying the parameters P_0 and T_0 the same trends in the details of the diffraction pattern were consistently reproduced: an increase in P_0T_0 enhanced the diffraction peaks at larger angles, while decreasing the product tended to wash out the diffraction pattern here.

Since P_0T_0 is indicative of the size of the particles nucleated (Sec. II), it is natural to associate the changing structure with a size effect. Our results do not bear this out. While it is certainly true that larger particles are predominantly fcc—our early experience with argon as carrier gas produced large particles, invariably with fcc structure—the size range of the results here does not "divide up" between the structure types. We observe all three structures over much the same range of sizes and conclude, instead, that the variety of conditions under which particles are produced has a strong influence on their structure.

A phase diagram for small metal particles, as a function of temperature and size, has been calculated by Ajayan and Marks in an attempt to explain structure changes in small gold particles observed in real time by high-resolution electron microscopy.[42] Their results show that, for a given size, a change in dominant structure—from fcc crystals, through decahedra, to icosahedra—should occur over a temperature range of several hundred degrees kelvin. Such behavior is qualitatively in agreement with our own experience. Reducing T_0, which will directly influence the temperature of the carrier gas inside the source, tends to change the diffraction pattern by reducing the detail at larger angles. This, we have shown, is indicative of a change towards decahedral and icosahedral structures. Furthermore, we note that in our results the decahedra appear first in the company of fcc domains (Figs. 6 and 7), then shift to icosahedral domains (Fig. 8), before diminishing in importance as icosahedra dominate (Fig. 9), suggesting that decahedra may well be dominant somewhere between the conditions that favor fcc crystals and icosahedra.

VI. CONCLUSIONS

The combination of electron diffraction and the inert-gas aggregation method of particle production has successfully provided a technique with which to study the structure of ultrafine silver particles. Not only are particles produced free of interaction with a support, but in the short time between their formation and their measurement they are unlikely to be affected by residual contaminants in the vacuum system. The technique is very sensitive to the diffracted intensity from small particles because the background, due to the diffraction from the carrier and residual gases, is weak and featureless and is relatively straightforward to correct for.

The dispersion in particle sizes must be taken into account when trying to identify the constituent structures. If it is not, size-dependent features, which are prominent in such small particles, will falsify any attempt to match experimental diffraction data with calculated patterns based on proposed models of local structure. In fact, these same size-dependent features have made it possible to identify not only the dominant structures in the particle beam, but also to estimate their size distributions.

Multiply twinned particles have been clearly identified in the beam, and, as source conditions are changed, a progression of structures has been observed: fcc domains are dominant when the temperature and pressure in the source are high; then, as P_0T_0 is reduced, a mixture of decahedra and fcc domains appear, followed by a mixture of decahedra with icosahedra, until finally icosahedra dominate the beam. In spite of the uncertain conditions of nucleation and growth in the source, our observations are in qualitative accord with the phase diagram proposed by Ajayan and Marks for small metal particles.[42] Their calculations predict that small metal particles will favor the icosahedral structure at lower temperatures, fcc structure at higher temperatures, and decahedral structures as an intermediary. We observe a tendency towards decahedral and icosahedral forms as source temperature is reduced. Furthermore, the decahedral structure is only observed in the presence of either fcc structure or icosahedra, but not both, suggesting that the conditions favoring the formation of decahedra are intermediate between those for fcc and icosahedral particles.

ACKNOWLEDGMENTS

We thank A. Hoareau for his help and encouragement during the experimental phase of this work, and the Swiss National Research Foundation for their financial support (Grant No. 20-26 535.89).

[1]S. Ino, J. Phys. Soc. Jpn. **21**, 346 (1966).
[2]J. G. Allpress and J. V. Sanders, Surf. Sci. **7**, 1 (1967).
[3]A. L. Mackay, Acta Crystallogr. **15**, 916 (1962).
[4]B. G. Bagley, Nature (London) **208**, 674 (1965).
[5]C. Y. Yang, J. Cryst. Growth **47**, 274 (1979).
[6]S. Ino, J. Phys. Soc. Jpn. **27**, 941 (1969).
[7]J. G. Allpress and J. V. Sanders, Austr. J. Phys. **23**, 23 (1970).
[8]L. D. Marks, Philos. Mag. **49**, 81 (1984).
[9]A. Howie and L. D. Marks, Philos. Mag. **49**, 95 (1984).
[10]K. Kimoto and I. Nishida, J. Phys. Soc. Jpn. **22**, 940 (1967).
[11]T. Hayashi, T. Ohno, S. Yatsuya, and R. Uyeda, Jpn. J. Appl. Phys. **16**, 705 (1977).
[12]Y. Saito, S. Yatsuya, K. Mihama, and R. Uyeda, J. Cryst. Growth **45**, 501 (1978).
[13]J. Farges, M. F. de Feraudy, B. Raoult, and G. Torchet, J. Chem. Phys. **78**, 5067 (1983).
[14]A. Yokozeki and G. D. Stein, J. Appl. Phys. **49**, 2224 (1978).
[15]B. G. de Boer and G. D. Stein, Surf. Sci. **106**, 84 (1981).
[16]L. D. Marks and D. J. Smith, J. Cryst. Growth **54**, 425 (1981).
[17]D. J. Smith and L. D. Marks, J. Cryst. Growth **54**, 433 (1981).
[18]C. Solliard, Rev. Sci. Instrum. **52**, 1321 (1981).
[19]C. Solliard, thèse No. 497, Ecole Polytechnique Fédérale de Lausanne, 1983 (unpublished).
[20]M. Flüeli, thèse No. 796, Ecole Polytechnique Fédérale de Lausanne, 1989 (unpublished).
[21]P. Mélinon, thèse No. 8635, Universitè Claude Bernard Lyon I, 1986 (unpublished).
[22]B. Hall, Rev. Sci. Instrum. **57**, 695 (1986).
[23]B. Hall, Comput. Phys. Commun. (to be published).
[24]N. Wada, Jpn. J. Appl. Phys. **7**, 1287 (1968).
[25]F. Frank, W. Schulze, B. Tesche, J. Urban, and B. Winter, Surf. Sci. **156**, 90 (1985).
[26]A. Guinier, *Théorie et Technique de la Radiocristallographie* (Dunod, Paris, 1964).
[27]H. Poppa, R. D. Moorhead, and M. Avalos-Borja, J. Vac. Sci. Technol. A **7**, 2882 (1989).
[28]H. P. Klug and L. E. Alexander, *X-Ray Diffraction Procedures for Polycrystalline and Amorphous Materials* (Wiley, London, 1974).
[29]G. J. Daniell and J. A. Potton, in *Maximum Entropy and Bayesian Methods,* edited by J. Skilling (Kluwer Academic, Dordrecht, The Netherlands, 1989), p. 151.
[30]C. W. B. Grigson and E. Barton, Brit. J. Appl. Phys. **18**, 175 (1967).
[31]C. L. Briant and J. J. Burton, Surf. Sci. **151**, 345 (1975).
[32]G. S. Cargill III, in *Solid State Physics,* edited by H. Ehrenreich, F. Seitz, and D. Turnbull (Academic, New York, 1975), Vol. 30, p. 227.
[33]F. L. Galeener and M. M. Rodoni, in *Amorphous and Liquid Semiconductors,* edited by J. Stuke and W. Brenig (Taylor and Francis, London, 1974), p. 101.
[34]F. Betts and A. Bienenstock, J. Appl. Phys. **43**, 4591 (1972).
[35]B. Hall, M. Flüeli, R. Monot, and J.-P. Borel, Helv. Phys. Acta **61**, 193 (1988).
[36]M. S. Cacei and W. P. Cacheris, BYTE **9** (5), 340 (1984).
[37]W. H. Press, B. P. Flannery, S. A. Teukolsky, and W. T. Vetterling, *Numerical Recipes: The Art of Scientific Computing* (Cambridge University Press, New York, 1986).
[38]S. Kirkpatrick, C. D. Gelatt, Jr., and M. P. Vecchi, Science **220**, 671 (1983).
[39]S. Ergun, Phys. Rev. B **1**, 3371 (1970).
[40]M. Blackman, Proc. R. Soc. London **173**, 68 (1939).
[41]J. M. Cowley, *Diffraction Physics* (North-Holland, New York, 1981).
[42]P. M. Ajayan and L. D. Marks, Phys. Rev. Lett. **60**, 585 (1988).